Efficient reduction of speckle noise in Optical Coherence Tomography

Maciej Szkulmowski, Iwona Gorczynska, Daniel Szlag, Marcin Sylwestrzak, Andrzej Kowalczyk, and Maciej Wojtkowski*

Institute of Physics, Nicolaus Copernicus University, ul. Grudziądzka 5/7, PL-87-100 Toruń, Poland
*Maciej.Wojtkowski@fizyka.umk.pl

Abstract: Speckle pattern, which is inherent in coherence imaging, influences significantly axial and transversal resolution of Optical Coherence Tomography (OCT) instruments. The well known speckle removal techniques are either sensitive to sample motion, require sophisticated and expensive sample tracking systems, or involve sophisticated numerical procedures. As a result, their applicability to *in vivo* real-time imaging is limited. In this work, we propose to average multiple A-scans collected in a fully controlled way to reduce the speckle contrast. This procedure involves non-coherent averaging of OCT A-scans acquired from adjacent locations on the sample. The technique exploits scanning protocol with fast beam deflection in the direction perpendicular to lateral dimension of the cross-sectional image. Such scanning protocol reduces the time interval between A-scans to be averaged to the repetition time of the acquisition system. Consequently, the averaging algorithm is immune to bulk motion of an investigated sample, does not require any sophisticated data processing to align cross-sectional images, and allows for precise control of lateral shift of the scanning beam on the object. The technique is tested with standard Spectral OCT system with an extra resonant scanner used for rapid beam deflection in the lateral direction. Ultrahigh speed CMOS camera serves as a detector and acquires 200,000 spectra per second. A dedicated A-scan generation algorithm allows for real-time display of images with reduced speckle contrast at 6 frames/second. This technique is applied to *in vivo* imaging of anterior and posterior segments of the human eye and human skin.

OCIS codes: (170.4500) Optical coherence tomography; (170.3880) Medical and biological imaging; (030.6140) Speckle; (350.5730) Resolution; (100.6950) Tomographic image processing.

References and links

1. D. Huang, E. A. Swanson, C. P. Lin, J. S. Schuman, W. G. Stinson, W. Chang, M. R. Hee, T. Flotte, K. Gregory, C. A. Puliafito, and J. G. Fujimoto, "Optical coherence tomography," Science **254**(5035), 1178–1181 (1991).
2. A. F. Fercher, C. K. Hitzenberger, G. Kamp, and S. Y. Elzaiat, "Measurement of intraocular distances by backscattering spectral interferometry," Opt. Commun. **117**(1-2), 43–48 (1995).
3. M. Wojtkowski, "High-speed optical coherence tomography: basics and applications," Appl. Opt. **49**(16), D30–D61 (2010).
4. P. Targowski, M. Iwanicka, L. Tymińska-Widmer, M. Sylwestrzak, and E. A. Kwiatkowska, "Structural examination of easel paintings with optical coherence tomography," Acc. Chem. Res. **43**(6), 826–836 (2010).
5. D. C. Adler, R. Huber, and J. G. Fujimoto, "Phase-sensitive optical coherence tomography at up to 370,000 lines per second using buffered Fourier domain mode-locked lasers," Opt. Lett. **32**(6), 626–628 (2007).
6. B. Potsaid, I. Gorczynska, V. J. Srinivasan, Y. L. Chen, J. Jiang, A. Cable, and J. G. Fujimoto, "Ultrahigh speed spectral / Fourier domain OCT ophthalmic imaging at 70,000 to 312,500 axial scans per second," Opt. Express **16**(19), 15149–15169 (2008).

7. R. J. Zawadzki, B. Cense, Y. Zhang, S. S. Choi, D. T. Miller, and J. S. Werner, "Ultrahigh-resolution optical coherence tomography with monochromatic and chromatic aberration correction," Opt. Express **16**(11), 8126–8143 (2008).
8. J. W. Goodman, "Some fundamental properties of speckle," J. Opt. Soc. Am. **66**(11), 1145–1150 (1976).
9. J. M. Schmitt, S. H. Xiang, and K. M. Yung, "Speckle in optical coherence tomography," J. Biomed. Opt. **4**(1), 95–105 (1999).
10. M. Bashkansky and J. Reintjes, "Statistics and reduction of speckle in optical coherence tomography," Opt. Lett. **25**(8), 545–547 (2000).
11. B. Karamata, K. Hassler, M. Laubscher, and T. Lasser, "Speckle statistics in optical coherence tomography," J. Opt. Soc. Am. A **22**(4), 593–596 (2005).
12. D. D. Duncan, S. J. Kirkpatrick, and R. K. K. Wang, "Statistics of local speckle contrast," J. Opt. Soc. Am. A **25**(1), 9–15 (2008).
13. K. W. Gossage, T. S. Tkaczyk, J. J. Rodriguez, and J. K. Barton, "Texture analysis of optical coherence tomography images: feasibility for tissue classification," J. Biomed. Opt. **8**(3), 570–575 (2003).
14. M. Szkulmowski, M. Wojtkowski, B. Sikorski, T. Bajraszewski, V. J. Srinivasan, A. Szkulmowska, J. J. Kałuzny, J. G. Fujimoto, and A. Kowalczyk, "Analysis of posterior retinal layers in spectral optical coherence tomography images of the normal retina and retinal pathologies," J. Biomed. Opt. **12**(4), 041207 (2007).
15. R. J. Zawadzki, A. R. Fuller, D. F. Wiley, B. Hamann, S. S. Choi, and J. S. Werner, "Adaptation of a support vector machine algorithm for segmentation and visualization of retinal structures in volumetric optical coherence tomography data sets," J. Biomed. Opt. **12**(4), 041206 (2007).
16. P. Yu, L. Peng, M. Mustata, J. J. Turek, M. R. Melloch, and D. D. Nolte, "Time-dependent speckle in holographic optical coherence imaging and the health of tumor tissue," Opt. Lett. **29**(1), 68–70 (2004).
17. A. Mariampillai, M. K. K. Leung, M. Jarvi, B. A. Standish, K. Lee, B. C. Wilson, A. Vitkin, and V. X. D. Yang, "Optimized speckle variance OCT imaging of microvasculature," Opt. Lett. **35**(8), 1257–1259 (2010).
18. A. Mariampillai, B. A. Standish, E. H. Moriyama, M. Khurana, N. R. Munce, M. K. K. Leung, J. Jiang, A. Cable, B. C. Wilson, I. A. Vitkin, and V. X. D. Yang, "Speckle variance detection of microvasculature using swept-source optical coherence tomography," Opt. Lett. **33**(13), 1530–1532 (2008).
19. V. J. Srinivasan, S. Sakadžić, I. Gorczynska, S. Ruvinskaya, W. C. Wu, J. G. Fujimoto, and D. A. Boas, "Quantitative cerebral blood flow with optical coherence tomography," Opt. Express **18**(3), 2477–2494 (2010).
20. J. K. Barton and S. Stromski, "Flow measurement without phase information in optical coherence tomography images," Opt. Express **13**(14), 5234–5239 (2005).
21. S. J. Kirkpatrick, R. K. Wang, and D. D. Duncan, "OCT-based elastography for large and small deformations," Opt. Express **14**(24), 11585–11597 (2006).
22. J. M. Schmitt, "OCT elastography: imaging microscopic deformation and strain of tissue," Opt. Express **3**(6), 199–211 (1998).
23. S. J. Kirkpatrick, D. D. Duncan, R. K. Wang, and M. T. Hinds, "Quantitative temporal speckle contrast imaging for tissue mechanics," J. Opt. Soc. Am. A **24**(12), 3728–3734 (2007).
24. A. E. Desjardins, B. J. Vakoc, A. Bilenca, G. J. Tearney, and B. E. Bouma, "Estimation of the scattering coefficients of turbid media using angle-resolved optical frequency-domain imaging," Opt. Lett. **32**(11), 1560–1562 (2007).
25. A. I. Kholodnykh, I. Y. Petrova, K. V. Larin, M. Motamedi, and R. O. Esenaliev, "Precision of measurement of tissue optical properties with optical coherence tomography," Appl. Opt. **42**(16), 3027–3037 (2003).
26. M. Pircher, E. Götzinger, R. Leitgeb, A. F. Fercher, and C. K. Hitzenberger, "Measurement and imaging of water concentration in human cornea with differential absorption optical coherence tomography," Opt. Express **11**(18), 2190–2197 (2003).
27. T. Støren, A. Røyset, L. O. Svaasand, and T. Lindmo, "Functional imaging of dye concentration in tissue phantoms by spectroscopic optical coherence tomography," J. Biomed. Opt. **10**(2), 024037 (2005).
28. T. R. Hillman, A. Curatolo, B. F. Kennedy, and D. D. Sampson, "Detection of multiple scattering in optical coherence tomography by speckle correlation of angle-dependent B-scans," Opt. Lett. **35**(12), 1998–2000 (2010).
29. Y. T. Pan, Z. L. Wu, Z. J. Yuan, Z. G. Wang, and C. W. Du, "Subcellular imaging of epithelium with time-lapse optical coherence tomography," J. Biomed. Opt. **12**(5), 050504 (2007).
30. D. Cabrera Fernández, H. M. Salinas, and C. A. Puliafito, "Automated detection of retinal layer structures on optical coherence tomography images," Opt. Express **13**(25), 10200–10216 (2005).
31. H. Tanna, A. M. Dubis, N. Ayub, D. M. Tait, J. Rha, K. E. Stepien, and J. Carroll, "Retinal imaging using commercial broadband optical coherence tomography," Br. J. Ophthalmol. **94**(3), 372–376 (2010).
32. A. E. Desjardins, B. J. Vakoc, G. J. Tearney, and B. E. Bouma, "Backscattering spectroscopic contrast with angle-resolved optical coherence tomography," Opt. Lett. **32**(21), 3158–3160 (2007).
33. S. G. Adie, T. R. Hillman, and D. D. Sampson, "Detection of multiple scattering in optical coherence tomography using the spatial distribution of Stokes vectors," Opt. Express **15**(26), 18033–18049 (2007).
34. J. Rogowska and M. E. Brezinski, "Evaluation of the adaptive speckle suppression filter for coronary optical coherence tomography imaging," IEEE Trans. Med. Imaging **19**(12), 1261–1266 (2000).
35. D. C. Adler, T. H. Ko, and J. G. Fujimoto, "Speckle reduction in optical coherence tomography images by use of a spatially adaptive wavelet filter," Opt. Lett. **29**(24), 2878–2880 (2004).

36. A. Ozcan, A. Bilenca, A. E. Desjardins, B. E. Bouma, and G. J. Tearney, "Speckle reduction in optical coherence tomography images using digital filtering," J. Opt. Soc. Am. A **24**(7), 1901–1910 (2007).
37. P. Puvanathasan and K. Bizheva, "Speckle noise reduction algorithm for optical coherence tomography based on interval type II fuzzy set," Opt. Express **15**(24), 15747–15758 (2007).
38. M. Gargesha, M. W. Jenkins, A. M. Rollins, and D. L. Wilson, "Denoising and 4D visualization of OCT images," Opt. Express **16**(16), 12313–12333 (2008).
39. S. Chitchian, M. A. Fiddy, and N. M. Fried, "Denoising during optical coherence tomography of the prostate nerves via wavelet shrinkage using dual-tree complex wavelet transform," J. Biomed. Opt. **14**(1), 014031 (2009).
40. Z. P. Jian, Z. X. Yu, L. F. Yu, B. Rao, Z. P. Chen, and B. J. Tromberg, "Speckle attenuation in optical coherence tomography by curvelet shrinkage," Opt. Lett. **34**(10), 1516–1518 (2009).
41. Z. P. Jian, L. F. Yu, B. Rao, B. J. Tromberg, and Z. P. Chen, "Three-dimensional speckle suppression in Optical Coherence Tomography based on the curvelet transform," Opt. Express **18**(2), 1024–1032 (2010).
42. K. M. Yung, S. L. Lee, and J. M. Schmitt, "Phase-domain processing of optical coherence tomography images," J. Biomed. Opt. **4**(1), 125–136 (1999).
43. A. Wong, A. Mishra, K. Bizheva, and D. A. Clausi, "General Bayesian estimation for speckle noise reduction in optical coherence tomography retinal imagery," Opt. Express **18**(8), 8338–8352 (2010).
44. D. L. Marks, T. S. Ralston, and S. A. Boppart, "Speckle reduction by I-divergence regularization in optical coherence tomography," J. Opt. Soc. Am. A **22**(11), 2366–2371 (2005).
45. J. M. Schmitt, "Array detection for speckle reduction in optical coherence microscopy," Phys. Med. Biol. **42**(7), 1427–1439 (1997).
46. H. W. Ren, Z. H. Ding, Y. H. Zhao, J. J. Miao, J. S. Nelson, and Z. P. Chen, "Phase-resolved functional optical coherence tomography: simultaneous imaging of in situ tissue structure, blood flow velocity, standard deviation, birefringence, and Stokes vectors in human skin," Opt. Lett. **27**(19), 1702–1704 (2002).
47. M. Pircher, E. Gotzinger, R. Leitgeb, A. F. Fercher, and C. K. Hitzenberger, "Speckle reduction in optical coherence tomography by frequency compounding," J. Biomed. Opt. **8**(3), 565–569 (2003).
48. B. Karamata, P. Lambelet, M. Laubscher, R. P. Salathé, and T. Lasser, "Spatially incoherent illumination as a mechanism for cross-talk suppression in wide-field optical coherence tomography," Opt. Lett. **29**(7), 736–738 (2004).
49. J. Kim, D. T. Miller, E. Kim, S. Oh, J. Oh, and T. E. Milner, "Optical coherence tomography speckle reduction by a partially spatially coherent source," J. Biomed. Opt. **10**(6), 064034 (2005).
50. T. M. Jørgensen, J. Thomadsen, U. Christensen, W. Soliman, and B. Sander, "Enhancing the signal-to-noise ratio in ophthalmic optical coherence tomography by image registration--method and clinical examples," J. Biomed. Opt. **12**(4), 041208 (2007).
51. Z. J. Yuan, B. Chen, H. G. Ren, and Y. T. Pan, "On the possibility of time-lapse ultrahigh-resolution optical coherence tomography for bladder cancer grading," J. Biomed. Opt. **14**(5), 050502 (2009).
52. S. Marschall, T. Klein, W. Wieser, B. R. Biedermann, K. Hsu, K. P. Hansen, B. Sumpf, K.-H. Hasler, G. Erbert, O. B. Jensen, C. Pedersen, R. Huber, and P. E. Andersen, "Fourier domain mode-locked swept source at 1050 nm based on a tapered amplifier," Opt. Express **18**(15), 15820–15831 (2010).
53. R. K. K. Wang and Z. H. Ma, "Real-time flow imaging by removing texture pattern artifacts in spectral-domain optical Doppler tomography," Opt. Lett. **31**(20), 3001–3003 (2006).
54. D. X. Hammer, R. D. Ferguson, N. V. Iftimia, T. Ustun, G. Wollstein, H. Ishikawa, M. L. Gabriele, W. D. Dilworth, L. Kagemann, and J. S. Schuman, "Advanced scanning methods with tracking optical coherence tomography," Opt. Express **13**(20), 7937–7947 (2005).
55. M. Hangai, M. Yamamoto, A. Sakamoto, and N. Yoshimura, "Ultrahigh-resolution versus speckle noise-reduction in spectral-domain optical coherence tomography," Opt. Express **17**(5), 4221–4235 (2009).
56. Heidelberg Engineering, "Spectralis," http://www.heidelbergengineering.com/products/spectralis-models/.
57. N. Iftimia, B. E. Bouma, and G. J. Tearney, "Speckle reduction in optical coherence tomography by "path length encoded" angular compounding," J. Biomed. Opt. **8**(2), 260–263 (2003).
58. H. Wang and A. M. Rollins, "Speckle reduction in optical coherence tomography using angular compounding by B-scan Doppler-shift encoding," J. Biomed. Opt. **14**(3), 030512 (2009).
59. A. E. Desjardins, B. J. Vakoc, W. Y. Oh, S. M. R. Motaghiannezam, G. J. Tearney, and B. E. Bouma, "Angle-resolved optical coherence tomography with sequential angular selectivity for speckle reduction," Opt. Express **15**(10), 6200–6209 (2007).
60. M. Hughes, M. Spring, and A. Podoleanu, "Speckle noise reduction in optical coherence tomography of paint layers," Appl. Opt. **49**(1), 99–107 (2010).
61. D. P. Popescu, M. D. Hewko, and M. G. Sowa, "Speckle noise attenuation in optical coherence tomography by compounding images acquired at different positions of the sample," Opt. Commun. **269**(1), 247–251 (2007).
62. B. F. Kennedy, T. R. Hillman, A. Curatolo, and D. D. Sampson, "Speckle reduction in optical coherence tomography by strain compounding," Opt. Lett. **35**(14), 2445–2447 (2010).
63. B. H. Park, M. C. Pierce, B. Cense, and J. F. de Boer, "Speckle averaging for optical coherence tomography by vibration of a thin water film," Proc. SPIE **5316**, 391–396 (2004).
64. I. Grulkowski, I. Gorczynska, M. Szkulmowski, D. Szlag, A. Szkulmowska, R. A. Leitgeb, A. Kowalczyk, and M. Wojtkowski, "Scanning protocols dedicated to smart velocity ranging in spectral OCT," Opt. Express **17**(26), 23736–23754 (2009).

65. T. Bajraszewski, M. Wojtkowski, M. Szkulmowski, A. Szkulmowska, R. Huber, and A. Kowalczyk, "Improved spectral optical coherence tomography using optical frequency comb," Opt. Express **16**(6), 4163–4176 (2008).
66. M. Gora, K. Karnowski, M. Szkulmowski, B. J. Kaluzny, R. Huber, A. Kowalczyk, and M. Wojtkowski, "Ultra high-speed swept source OCT imaging of the anterior segment of human eye at 200 kHz with adjustable imaging range," Opt. Express **17**(17), 14880–14894 (2009).
67. B. Cense, N. A. Nassif, T. C. Chen, M. C. Pierce, S.-H. Yun, B. H. Park, B. E. Bouma, G. J. Tearney, and J. F. de Boer, "Ultrahigh-resolution high-speed retinal imaging using spectral-domain optical coherence tomography," Opt. Express **12**(11), 2435–2447 (2004).
68. M. Wojtkowski, V. J. Srinivasan, T. H. Ko, J. G. Fujimoto, A. Kowalczyk, and J. S. Duker, "Ultrahigh-resolution, high-speed, Fourier domain optical coherence tomography and methods for dispersion compensation," Opt. Express **12**(11), 2404–2422 (2004).
69. M. Szkulmowski, A. Szkulmowska, T. Bajraszewski, A. Kowalczyk, and M. Wojtkowski, "Flow velocity estimation using joint Spectral and Time domain Optical Coherence Tomography," Opt. Express **16**(9), 6008–6025 (2008).
70. M. Szkulmowski, I. Grulkowski, D. Szlag, A. Szkulmowska, A. Kowalczyk, and M. Wojtkowski, "Flow velocity estimation by complex ambiguity free joint Spectral and Time domain Optical Coherence Tomography," Opt. Express **17**(16), 14281–14297 (2009).
71. A. E. Desjardins, B. J. Vakoc, G. J. Tearney, and B. E. Bouma, "Speckle reduction in OCT using massively-parallel detection and frequency-domain ranging," Opt. Express **14**(11), 4736–4745 (2006).
72. J. W. Goodman, *Statistical Optics* (Wiley, New York, 2000).
73. B. J. Vakoc, G. J. Tearney, and B. E. Bouma, "Statistical properties of phase-decorrelation in phase-resolved Doppler optical coherence tomography," IEEE Trans. Med. Imaging **28**(6), 814–821 (2009).
74. R. K. Wang and Z. Ma, "Real-time flow imaging by removing texture pattern artifacts in spectral-domain optical Doppler tomography," Opt. Lett. **31**(20), 3001–3003 (2006).
75. S. H. Yun, G. J. Tearney, J. F. de Boer, and B. E. Bouma, "Motion artifacts in optical coherence tomography with frequency-domain ranging," Opt. Express **12**(13), 2977–2998 (2004).

1. Introduction

Optical Coherence Tomography (OCT) is a rapidly developing imaging modality which allows for noninvasive cross-sectional imaging of weakly scattering, semitransparent samples with high sensitivity [1–3]. It has been successfully applied as an imaging tool in medical [3] or material studies [4]. OCT with Fourier domain detection can reach imaging speeds up to several hundred thousand lines per second [5,6]. This method offers also high resolution of imaging up to few microns in both axial and lateral directions [7]. The axial resolution in OCT is determined by spectral properties of the light source, while the lateral resolution depends, similarly to laser confocal microscope techniques, on the spot size of the focused illuminating light beam. Since OCT uses coherent illumination, the speckle pattern is another factor which limits, in both axial and lateral direction, effective image resolution, defined as the smallest detectable detail in an OCT [8–12].

Following Schmitt's paper from 1999, the speckle pattern has two main components: a signal-carrying speckle and a signal-degrading speckle [9]. The first is generated by single back scattering of the incident light, while the latter is generated due to interference of photons multiply scattered in reverse and forward direction. The resulting speckle pattern is visible in the image as a grainy structure which blurs structural details in the image, but the information encoded in its intensity and phase statistics may be used. This duality causes that the presence of the speckle field can be treated in two main ways. The first approach concentrates on the speckle suppression, while the second takes advantage of the speckle pattern statistics which depend on the internal structure size, position and the velocity of the scatterers inside the sample.

Speckle pattern statistics has been used in segmentation of different tissue layers visible in tomographic images [13–15] or in differentiating tumor from healthy tissue [16]. Since moving scattering particles cause a change in the degree of correlation between lines in OCT tomogram, it becomes feasible to extract blood flow in living tissue and to visualize the vascular network [17–19]. Quantitative flow measurement is still not possible using only speckle pattern statistics, but some preliminary results have already shown that in principle it should be possible to use these parameters as indicators for the total flow value [19,20]. Another application of speckle pattern analysis is optical elastography, in which position of

single speckles in the image is tracked as a function of pressure applied to the sample [21,22]. There were also attempts to measure mechanic, scattering and absorptive properties of samples using speckle pattern analysis [23–28].

Apart from carrying information, the speckle pattern may influence a correct interpretation of tomographic images, in such a case, speckle pattern is considered as noise. In retinal imaging speckles can mimic small structural features like capillaries [7] or cellular morphology details [29]. Retinal layer visibility and segmentation can be improved by the speckle reduction [30,31]. Additionally, the reduced speckle pattern caused by multiple scattering can improve the reliability of detecting scattering coefficient, as well as the spectroscopic analysis [24–26,32,33]. Because of that, several research groups and companies attempt to create techniques to decrease speckle noise (in other words: to decrease speckle pattern contrast) using either software or hardware solutions.

Software based speckle reduction techniques include: local averaging of pixels in axial and lateral direction [26], averaging with rotating kernels [34], wavelet transformations [35–39], curvlet transformations [40,41], phase adjustment procedures [42], numerical frequency compounding [9], adaptive estimation of noise-free data using nonlinear Bayesian least square estimation [43], image regularization [44], or filtering the tomograms using filters: adaptive [9], median, Lee, symmetric nearest neighbor, Wiener [36], and anisotropic diffusion [30,37]. The abovementioned attempts to reduce speckle noise by application of sophisticated numerical algorithms face the problem of high computation needs and/or reduction of resolution of the images. The main advantage of these approaches is that they can be applied to almost all 2D and 3D images acquired by any OCT device.

Hardware based techniques require a modification in optical setup or a change in scanning protocols to acquire a number of tomograms with uncorrelated speckle patterns. These tomograms are averaged to obtain final images with reduced speckle contrast. The main challenge of these methods is to acquire the images in such a way that the speckle pattern differs, but the indispensable change of the imaged structure is as small as possible. The change in the imaged structure has to be chosen carefully, because averaging may lead to a significant loss of resolution. Therefore, it is necessary to understand the specific morphology of the imaged object to predetermine the extent of information loss caused by the speckle averaging procedure. Hardware speckle reduction techniques are particularly promising, since in principle they can offer minimal possible lateral resolution drop in the images. Uncorrelated speckle patterns can be obtained by means of time, space, optical frequency, or polarization diversity [8]. All of these approaches have been already applied for speckle suppression in OCT imaging. It is convenient to divide hardware techniques into serial and parallel.

The parallel hardware speckle reduction methods acquire tomograms with different speckle patterns used for averaging at the same time. Several ways to achieve this goal have been reported up to date. Differentiation of the speckle patterns has been achieved by application of light with different polarizations emitted by two sources [45,46], by optical frequency compounding with two incoherent interferometric signals using two light sources with different central wavelengths [47], or with a partially spatially coherent light source [48,49]. The main advantage of these techniques is that there is almost no lateral resolution loss. However, the detection systems have to be multiplied, and the speckle reduction ratio is limited, since only a few independent speckle patterns can be acquired.

The serial techniques are simpler and more popular. The basic principle underlying these methods is the acquisition of several tomograms in consecutive time intervals from the same location in the sample, but with slightly changed ensemble of the illuminated scattering particles.

In the most straightforward realization of this idea, two- or three-dimensional images are collected one after another with scanning beam shifted laterally on the sample. The shift is usually accomplished by exploiting instability of the setup and the sample (bulk-motion), with

no intentional beam deflection [7,50–52]. A variant of this approach has been used for despeckling Doppler OCT images, when two tomograms were acquired with scanning in opposite directions [53]. Prior to averaging, the tomograms have to be properly aligned. Because of the bulk-motion, sophisticated algorithms need to be used to align the tomograms before averaging to compensate random motion of the sample that introduces macroscopic shifts in axial and lateral directions [50]. All uncompensated shifts of the sample decrease the lateral resolution in the final tomogram. A common problem for this kind of techniques is that the lateral displacement between A-scans remains unknown due to the unknown amplitude of bulk motion of the object. Additionally, the performance of the techniques depends strongly on the acquisition time of the entire tomogram. Therefore, for cross-sectional images with a large number of lines it may be difficult or impossible to align the tomograms [29]. In ophthalmic applications of OCT, an eye-tracker may be incorporated to the instrument to minimize randomness in lateral displacement, consequently improving the overall repeatability [54,55]. Unfortunately, since eye-tracking devices compensate only for lateral displacements of the eye, numerical compensation of axial displacement is still required to precede tomogram averaging. Additionally, it is not certain yet whether even the use of advanced tracking system would allow for speckle reduced imaging in case of eyes with poor fixation [55]. Currently, an OCT system using this approach is offered commercially by Heidelberg Engineering in the Spectralis devices [56].

Another common approach of differentiating speckle pattern is averaging tomographic images acquired from different observation angles. There exist several modalities of this "angular compounding" technique which use path length encoding [57], Doppler encoding [58] or multiple backscattering angles encoding [10,59,60] to illuminate the sample from different angles. These approaches seem to give the possibility to remove the speckle with no loss of lateral resolution. Unfortunately, because of the unknown and uncontrollable shifts of the sample in case of *in vivo* imaging, there is a necessity to align tomograms prior to averaging, which is the same drawback as in the standard tomogram averaging techniques. Furthermore, severe changes in the setup, complicated acquisition procedures, and problems with sensitivity of the imaging resulted in the fact that *in vivo* imaging via these techniques has only been possible for human skin [57,59], and has not been applied in ophthalmic imaging.

There are also less common techniques of decorrelating speckle patterns, which include: changing the position of focal point inside the sample [61], application of external force to the sample [62] or imaging through thin water film [63], however, their applicability to *in vivo* imaging is limited.

In this contribution, we propose a technique for speckle contrast reduction by spatial compounding of tomographic images, which is insensitive to sample bulk motion and allows for precise control on lateral resolution and speckle contrast reduction. Additionally, it does not require any sophisticated algorithms to be used prior to averaging, what permits a real-time display of tomograms with reduced speckle contrast.

2. Materials and methods

2.1. Tomogram averaging method

The speckle contrast reduction technique, which we present in this article, uses different data acquisition paradigm than previously introduced modalities. The scanning pattern presented in this contribution is similar to segmented data acquisition protocols, which has been recently demonstrated by our group [64]. The shifts of the beams on the sample that lead to decorrelation of speckle patterns in consecutive A-scans are performed in the direction perpendicular to the plane of cross-section. The light beam trajectory on the sample is schematically illustrated in Fig. 1(a).
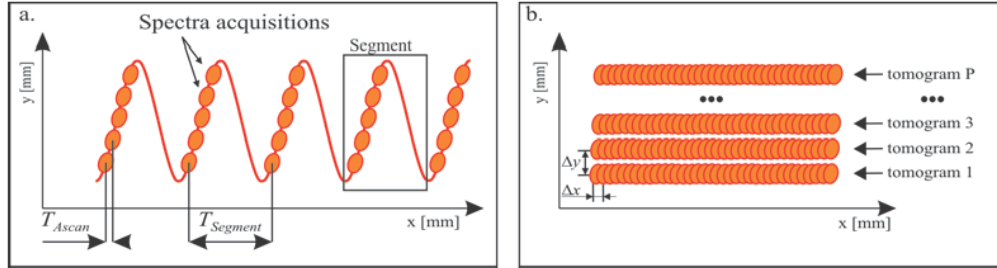
Fig. 1. **a.** Schematic drawing of light beam trajectory on the sample (solid line) with sparse sampling for explanatory purposes. Light beam is deflected in direction (y) perpendicular to lateral direction of the tomogram (x). Dots mark positions where consecutive spectra are acquired. A set of data called "segment" is acquired during one period ($T_{Segment}$) of lateral beam deflection. T_{Ascan} is repetition time of the spectra acquisition, **b.** Scanning pattern from a. with much denser sampling in lateral (x) direction, than in lateral (y) direction. Such sampling resembles more real experimental configuration; Δx and Δy are distances between acquired spectra in two lateral directions. See the text for more detailed description.

The scanning trajectory is composed of two independent and perpendicularly oriented components of light beam deflection. A fast oscillatory deflection in lateral (y) direction is superimposed on a relatively slow beam deflection in lateral (x) direction. Spectra acquired during one period $T_{Segment}$ of oscillatory movement define a data segment, as shown in Fig. 1(a). As it can be seen from Fig. 1(b), spectral fringe signals with the same indexes within consecutive segments can be regarded as belonging to tomograms laterally shifted in (y) direction. If the amplitude of the beam deflection in (y) direction, number of samples per segment and the beam width are chosen correctly, averaging of such tomograms will enable imaging with strongly reduced speckle noise. Additionally, since the beam deflection in two perpendicular directions can be performed by separate devices, the sampling density in both directions can be set independently. Specifically, sampling density in lateral (x) direction can be chosen adequately to allow also for Doppler imaging, as shown by Grulkowski et al. [64].

Because of the short acquisition time between consecutive A-scans within one segment, the beam shift on the sample between averaged tomograms is defined mostly by the amplitude of lateral deflection in (y) direction, and not by the sample motion. This makes the technique almost insensitive to undesired sample movements. Additionally, the degree of decorrelation is kept constant along lateral (y) direction of tomogram and can be altered by changing the deflection amplitude. This, in turn, makes it possible to control the tradeoff between the lateral resolution and the decorrelation of the speckle pattern. A strong advantage of the technique is that it decouples the degree of speckle contrast reduction from the number of lines in averaged tomograms, what allows for efficient despeckling of the tomograms. These advantages of the approach are discussed in more detail later in the text.

2.2. Experimental setup

In principle, the presented technique can be applied to any modality of Optical Coherence Tomography. In this study we show the results obtained with a standard Spectral OCT device in which the object arm is modified by the introduction of a resonant scanner (Fig. 2). The light source is a superluminescent diode (SLD-351-HP2-DBUT-SM-PD, Superlum, Russia) emitting at 820nm with the spectral bandwidth of 70 nm (full width at half maximum). The measured axial resolution is 5.7 μm in the air (~4.2 μm in tissue). After passing the isolator, the light splits in the fiber coupler into the reference and object arms of the Michelson interferometer. The splitting ratio was 80/20, correspondingly. In the reference arm we have implemented polarization control of light propagating in the fiber, light attenuation and dispersion compensation. The light emerging from the fiber is collimated with a 19mm focal length achromatic lens and directed to the resonant scanner with 4kHz scanning frequency

(CRS 4 kHz, Cambridge Technology). Two identical lenses (f = 50mm focal lengths) in 4f configuration relay the beam to the galvanometer scanners. Scan lens (f = 75mm) and objective lens (f = 50mm) allow for retinal imaging. Additional lens (f = 30mm) is inserted for imaging of the anterior segment of the eye and model objects. The measured beam diameter equals 15 µm. The spectrometer configuration uses a 1200 lpmm diffraction grating and a CMOS line scan camera (Sprint, Basler). To allow imaging with speeds up to 200,000 lines/s (5 µs repetition time) CMOS detector was set to acquire 1024 pixels.
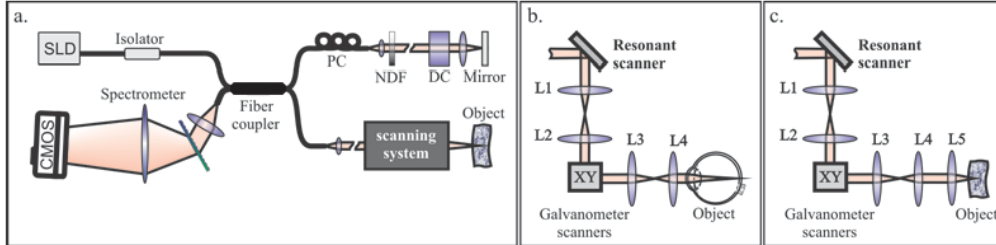
Fig. 2. **a.** Spectral OCT setup used in experiments. **b.** Scanning system for imaging the posterior chamber of the human eye. **c.** Scanning system for imaging phantoms, human skin and the anterior chamber of the human eye. SLD – superluminescent diode; PC – polarization controller; NDF – neutral density filter; DC – dispersion compensator; CMOS – camera; L1-5 – lenses.

To ensure that the averaging technique works properly, it is necessary that the acquisition of spectral fringe signals for each segment starts at the same phase of the resonant scanner deflection. Because the exact period of the resonant scanner and the sampling period of the CMOS camera do not have common multiples ($T_{segment} = 1/3938 \, s$), data acquisition in each segment needs to be synchronized with the resonant scanner oscillations, as shown in Fig. 3.
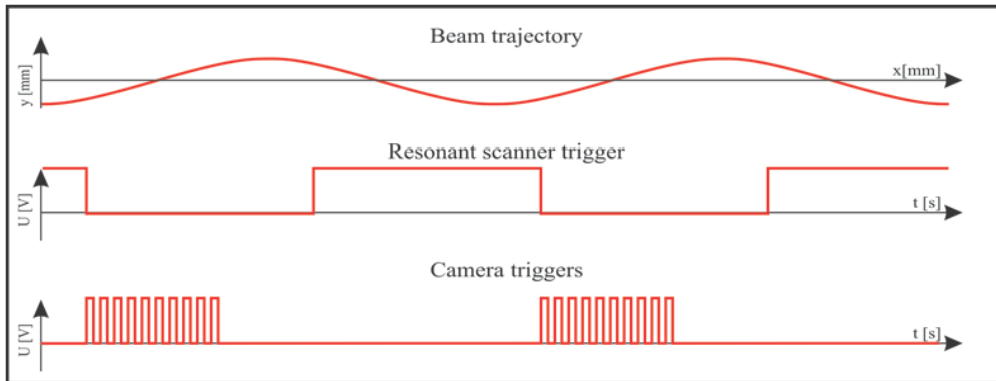

Fig. 3. Schematic plot of driving signals synchronization in the speckle reduction technique. See the text for details.

The synchronization is performed using High-Speed Analog Output NI PCI-6733 board (D/A) which captures the TTL signal generated by the scanner CRS Driving Board at the chosen position of the scanner mirror and sends a sequence of points from previously loaded galvanometric scanner trajectories and camera triggers to the scanners and the camera. The duration of the sequence is controlled by the sample clock frequency of the board and is set to be shorter than the resonant scanner period. The maximal number of image lines that can be acquired during one period of the resonant scanner depends on the repetition time (T_{Ascan}) of the camera. Up to 48 A-scans can be acquired with $T_{Ascan} = 5 \, \mu s$. In our experiments we use

16 spectra, from the linear part of one slope of the resonant scanner trajectory. The amplitude of the resonant scanner is set using independent channel on the D/A board.

2.3. Data processing

The signal and image processing are performed with a custom multithreaded application written entirely in C++ by authors of this manuscript. The application has been designed to work in three distinct modes. In the *Preview Mode*, which is used for alignment of the sample, two cross-sectional tomograms (horizontal and vertical) of the sample are displayed in real time. Each of the tomograms consists of 400 lines and one line is constructed by averaging 16 A-scans from one segment. During the *Measurement Mode* all acquired spectra are streamed to the disc. In the *Postprocessing Mode* the spectra saved previously to the disc are loaded, transformed to tomograms, displayed and saved.

The transfer of spectral fringe signals to RAM memory of the Personal Computer (from framegrabber or computer hard disc) is followed by the subtraction of the fixed pattern noise from each spectrum. This noise is computed as an average of many camera read-outs acquired when scanners are deflected-out from the object, so that neither signals from the sample nor residual noise components from an object are registered. This separate noise frame is acquired either after every pair of tomograms in the *Preview Mode*, or after all the tomograms are acquired during the *Measurement Mode*. The third step in the data processing is resampling the spectrum from pixel-space to k-space (wavenumber space). This procedure requires two additional Fourier transformations per spectrum which substantially increase the calculation time. In order to calculate fractional numbers of pixels equidistant in k-space, a comb-like spectrum of light after passing a Fabry-Perot interferometer is acquired [65]. Next, a procedure described in Ref. [66] is applied, but instead of the reference spectral fringe phase, numbers of comb peaks are used to compute the relation linking pixel number with wavenumber. The fourth step is dispersion correction, which is performed by simple multiplying resampled spectrum by a complex vector containing second order dispersion phase [67]. If the proper value of dispersion coefficient is chosen, one of complex conjugate images in the tomogram is sharpened, while the other suffers from doubled dispersion dependent worsening of the resolution [68]. The dispersion compensation procedure can be also used to perform a correction of axial position of the sample imaged on the tomogram, by adding a component linear with respect to wavenumber. The last step is Fourier transformation of all spectral fringe signals.

Finally, a line of cross-sectional image can be obtained by averaging in linear scale the amplitudes of A-scans obtained in previous steps. This can be done in two ways. In the first approach, averaging is performed on data taken from one segment, as shown in Fig. 1(a). This approach is used in the *Preview Mode*, where computational time efficiency is crucial. It has to be noted that in this approach there is no additional computation required, as compared to standard SOCT processing with averaging. In the second approach, the cross-sectional OCT images are created from A-scans collected at the same phase of the resonant scanner, and as a result they have identical positions (along lateral (y) direction) within the consecutive segments. This is schematically depicted in Fig. 1(b), where such A-scans are part of "tomogram 1," "tomogram 2," etc. Because spectral fringes acquired from adjacent segments can overlap, Doppler analysis is also possible in this approach. To obtain images with reduced speckle contrast, structural and Doppler tomograms are averaged. This approach is used only in the *Postprocessing Mode,* due to higher computational load connected with application of Spectral and Time domain OCT (STdOCT) which requires extra Fourier transformation along time axis [69,70] to calculate Doppler tomograms with high-sensitivity.

All the steps of the procedures are implemented with the use of Intel Performance Primitives® library and compiled with Intel Compiler® as 64-bit multithreaded application. Data frame corresponding to one cross-sectional image are divided into equisized data chunks which are processed simultaneously by different CPU threads. Computation performance of

the software allows for real-time display of tomograms with reduced speckle contrast in *Preview Mode* and with frame-rate of 6 frames per second for images containing 400 lines.

2.4. Quality of images with speckle pattern

The statistical properties of the speckle field in Optical Coherence Tomography have been discussed in detail in Refs. [8–12] and will not be repeated here. In this work we do not concentrate on the origins of speckles but we focus only on reduction of their influence on the image quality. In order to predict the speckle contrast reduction due to averaging we define $\overline{I_s}$, $\overline{I_n}$, σ_s, σ_n as amplitudes and standard deviations of signal and noise, respectively. Several parameters may be used to locally quantify speckle pattern in OCT images, such as the signal to noise ratio *SNR* [9,10,57,59,71] (squared *SNR* is called equivalent number of looks *ENL* [35,41]):

$$SNR = \sqrt{ENL} = \frac{\overline{I_s}}{\sigma_s} \tag{1}$$

or contrast of speckle pattern [8,47] (also referred to as speckle contrast [58], speckle contrast ratio [60] or relative standard error of the mean intensity [25]):

$$C = \frac{\sigma_s}{\overline{I_s}}. \tag{2}$$

Another parameter is a contrast to noise ratio [35,41]:

$$CNR = \frac{\overline{I_s} - \overline{I_n}}{\sqrt{\sigma_s^2 + \sigma_n^2}} \tag{3}$$

or alternatively [50]

$$CNR = \frac{2\left(\overline{I_s} - \overline{I_n}\right)^2}{\sigma_s^2 + \sigma_n^2}. \tag{4}$$

A different definition of signal to noise ratio is given in Ref. [35,41], where it is called a peak signal to noise ratio:

$$pSNR = \frac{\max\left(I_s\right)}{\sigma_n}. \tag{5}$$

One should notice that the *pSNR* calculated using the above definition depends on the speckle field in a different way than the *SNR* calculated using the definition from Eq. (1), and can be strongly influenced by signal spikes related to the speckles and noise. As a result, it may give overestimated values of signal to noise ratio. Therefore, we decided to use a different definition of the peak signal to noise. We define σ_s' as the signal amplitude variation in case no speckle is present. This cannot be measured directly, due to speckle related intensity fluctuations, but we use a relation that links speckle-free signal amplitude variation with the noise floor variation [72]:

$$pSNR = \frac{\overline{I_s}}{\sigma_s'} = \frac{\overline{I_s}}{\sigma_n} \cdot \sqrt{\frac{2}{4-\pi}} \cong \frac{\overline{I_s}}{\sigma_n} \cdot 1.526. \tag{6}$$

Such a definition of *pSNR* is decoupled from the speckle pattern and, as a result, gives information on overall sensitivity of the OCT system, which can vary with changes of scanning beam velocity in both lateral (x) and (y) directions.

The cross-correlation $XCOR$ values may be used as an indicator of similarity between different speckle fields [41,47] (σ_1 and σ_2 are standard deviations of different speckle patterns, while σ_{12} is the covariance between them):

$$XCOR = \frac{\sigma_{12}}{\sigma_1 \sigma_2}. \qquad (7)$$

Averaging is most efficient in the case of a complete decorrelation between speckle patterns $(XCOR = 0)$. In such a case, the signal to noise ratio SNR increases and speckle contrast C decreases with $\sqrt{P}$, where P is the number of averaged A-scans [8]. In this work we broaden this statistical approach of describing the measured speckle patterns (Eq. (7)), and derive a technique to predict the reduction of speckle contrast due to averaging as a function of scanning parameters. Figure 4 presents symbols used in the expressions below.
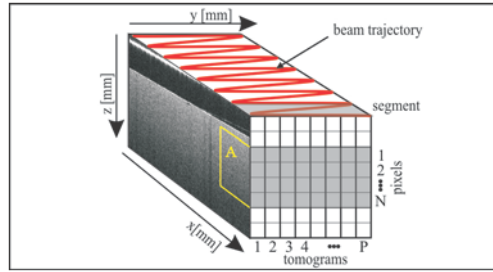
Fig. 4. Schematic drawing of a data set acquired for tomogram averaging with symbols used in the text.

We assume that the averaged A-scans are simply realizations of a random process with pixels from the same axial position correlated in some manner. In such an approach we can write an expression for the speckle pattern contrast after averaging P A-scans:

$$C_A = \frac{\sigma_A}{\overline{I}_A}, \qquad (8)$$

where the mean value $\overline{I}_A$ and the variance σ_A^2 are calculated for the averaged A-scans. We assume that locally, the properties of speckle pattern are stationary, so the contrast values calculated for area A (Fig. 4) are equal to the contrast values calculated from a single A-scan. The contrast for one tomogram line depends on the averaged A-scans from one segment. Therefore, the following calculations are performed for A-scans taken from one segment.

Using a definition of an expected value $Ex = N^{-1}\sum_{n=0}^{N-1} x(n)$, where N is a number of pixels and the index n enumerates these pixels in the A-scan to be analyzed, we can define

$$\overline{I}_A = EI_A, \qquad (9)$$

$$I_A(n) = \frac{1}{P}\sum_{p=0}^{P-1} I_p(n), \qquad (10)$$

$$\sigma_A^2 = E\left(I_A - \overline{I}_A\right)^2. \qquad (11)$$

The latter expression can be rewritten using variances and covariances of single A-scans:

$$\sigma_{pp} = \frac{1}{P^2} E\left(I_p - \overline{I}_p\right)\left(I_p - \overline{I}_p\right), \qquad (12)$$

$$\sigma_{pq} = \frac{1}{P^2} E\left(I_p - \overline{I}_p\right)\left(I_q - \overline{I}_q\right), \tag{13}$$

and takes the following form:

$$\sigma_A^2 = \sum_{p=0}^{P-1}\sum_{q=0}^{P-1}\sigma_{pq}. \tag{14}$$

In Eqs. (12-14) indexes p and q enumerate A-scans and $\overline{I}_p = EI_p$. We further rewrite this expression and group the covariances by distance between A-scans used to calculate them. Taking advantage of the fact that $\sigma_{pq} = \sigma_{qp}$ we obtain

$$\sigma_A^2 = \sum_{k=-P+1}^{P-1}\sum_{p=0}^{P-1-|k|}\sigma_{p,p+|k|}. \tag{15}$$

After defining a zero mean A-scan $Y_p(n) = I_p(n) - \overline{I}_p$, where $\overline{I}_p = EI_p$, and using definitions (12) and (13) we can rewrite Eq. (15):

$$\sigma_A^2 = \sum_{k=-P+1}^{P-1}\sum_{p=0}^{P-1-|k|}\frac{1}{P^2}E\left(Y_pY_{p+|k|}\right) = \frac{1}{P^2}E\sum_{k=-P+1}^{P-1}R_{YY}(k) = \sum_{k=-P+1}^{P-1}\overline{R}_{YY}(k), \tag{16}$$

where $R_{YY}(k) = \sum_{p=0}^{P-1-|k|}Y_pY_{p+|k|}$ is the estimate of the autocorrelation function of the object sampled at discrete points k which enumerates distances between A-scans in units of sampling positions. $\overline{R}_{YY}(k) = P^{-2}ER_{YY}(k)$ is $R_{YY}(k)$ scaled by number of A-scans and averaged over a range of in depth positions. This approach has the advantage of relying only on the experimental data and it inherently incorporates all the properties and aberrations of the optical setup and the sample that should be known in the case of a careful modeling of the speckle pattern [73]. Such a modeling is especially challenging in the case of imaging of posterior parts of the eye, since eye optics introduces unknown distortions in the wavefront of sampling beam, as well as in geometry of the scanning system. In our approach, the modeling is not required and the estimation of useful scanning range can be based solely on measurable data.

Equation (16) states that the variance σ_A^2 of the averaged A-scans can be calculated as an area under the curve of a scaled and averaged autocorrelation function $\overline{R}_{YY}(k)$. In order to minimize the variance σ_A^2, it is therefore necessary to sample the object in such positions of the beam for which this autocorrelation function becomes equal to or close to Dirac delta function. From the plot of the function $\overline{R}_{YY}(k)$, it is possible to read for which value of k the function vanishes to zero. Since the argument k of the autocorrelation function is simply the step of sampling beam on the object, it can be converted to any value convenient to operator, such as voltage applied to a resonant scanner or the similar. Consequently, the proper value of such a parameter which result in optimal scanning, can easily be found. The ability to choose optimal scanning parameters is crucial for the practical speckle reduction, as once the complete decorrelation between A-scans is obtained, further increase of distance between acquisition positions does not lead to any improvement in contrast of the speckle pattern, but only makes the lateral resolution worse.

3. Results and discussion

3.1. Phantom imaging

In order to experimentally verify the theoretical analysis presented in the previous section, we imaged a phantom of a drop of slightly scattering silicon covered with microscope cover glass, which was tilted with respect to the probing beam to minimize reflections. Such an object has stationary scattering properties and can be easily immobilized, so that the bulk motion has no influence on the correlation between A-scans to be averaged. In our current implementation of the technique, spectral fringe signals are acquired only when light beam is deflected in one direction along lateral (y) axis on the sample. This allows us to avoid problems with alignment of even and odd lines of the final cross-sectional image caused by imperfect synchronization of the data acquisition on the opposite sides of the segment trajectory. Because our electronics did not allow for perfect synchronization, we decided to acquire only a half of the possible spectral fringes within each segment. However, in principle it is possible to acquire spectral fringes also on the other half of the segment, what has extra advantage of the phase noise reduction [74] to improve Doppler analysis.

The scanning protocol used in the phantom imaging consists of 1000 segments and lateral measurement range was set to 800 µm. The total acquisition time per averaged tomogram is equal to 0.25 s, since in our technique it depends only on the number of segments and vibration frequency of the resonant scanner (in our experiments ~4 kHz). Most of the scatterers contributing to the speckle field are much smaller than the beam width [9]. Therefore, for fixed light wavelength, the speckle field depends on numerical aperture, scanning velocity in the lateral direction together with repetition and exposure times of the detector. For the experiment we fixed the numerical aperture and the size of the beam. We measured speckle contrast C (Eq. (2)), peak signal to noise ratio $pSNR$ (Eq. (6)) and contrast to noise ratio CNR (Eq. (3)) as a function of the total lateral beam deflection y_R, as shown in Fig. 5(a), for three different repetition times. The aim of the experiment was to find a combination of lateral beam deflection and repetition time, which optimize image quality, while assuring the smallest possible lateral resolution loss. To quantify image quality we choose contrast to noise ratio CNR.

Figure 5 shows the results of the speckle reduction technique applied to the scattering phantom. The time interval corresponding to acquisition of one data segment is approximately 250 µs, but data was acquired during a half of this time. We have tested three acquisition protocols fit to duration of 125 µs. We acquired: 24 A-scans with 5 µs repetition time (3.6 µs exposure time), 12 A-scans with 10 µs repetition time (8.6 µs exposure time) and 6 A-scans with 20 µs repetition (18.6 µs exposure time). Light beam trajectory is sinusoidal in shape, therefore, we averaged only spectra from this part of the light beam trajectory where relation between time and distance on the sample is linear: 16, 8 and 4 spectra respectively for the abovementioned patterns. Light power in the reference arm of the spectrometer was adjusted adequately to maximize sensitivity for each repetition time. Values of $pSNR$ defined by Eq. (6), drop down as the resonant scanner amplitude or the exposure time increases, as shown in Fig. 5(b). This effect is achieved because of the fringe washout which increases when scanning beam travels larger distances on the sample during acquisition [75]. As a result, the amplitude of the signal decreases, while the noise level and variance stay independent on scanning parameters (the noise background is always decorrelated). It is therefore advantageous to acquire as many spectral fringes as possible within one segment (or alternatively speaking, within the resonant scanner period).

Another observation is that the contrast of speckles C decreases as a function of beam deflection until it stabilizes for lateral beam deflection of approx. 100 µm. Further increase of the amplitude does not improve the result, as shown in Fig. 5(c). Looking on the plots presented in Fig. 5 it is possible to conclude that the contrast-to-noise ratio CNR is an

optimal parameter for quantification of the image quality improvement. Local maximum of CNR on Fig. 5(d) is reached for the optimal value of beam deflection for the speckle reduction, which in this particular case corresponds to the deflection amplitude of approx. 110 µm. Similarly to $pSNR$ and C, it is obvious here that it is advantageous to divide the segment period into highest possible number of acquisitions. The tomograms obtained with 4 µm, 110 µm (optimal) and 560 µm of the beam deflection are presented in Fig. 5(g), 5(h) and
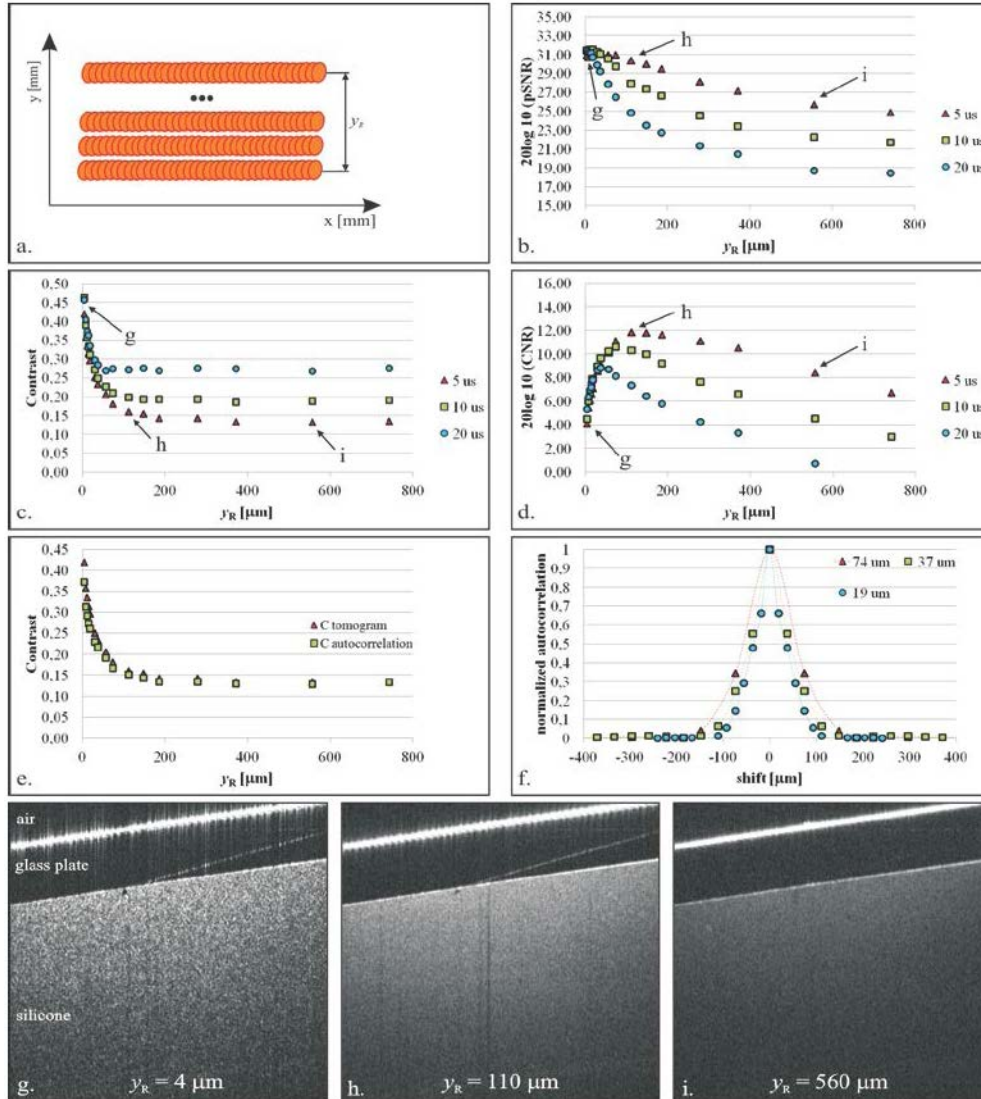
Fig. 5. Optimization of the speckle contrast reduction technique using scattering phantom. **a.** Schematic drawing of the scanning protocol indicating data used for averaging: y_R is the distance between the two cross-sectional images; **b.** peak signal-to-noise ratio ($pSNR$, Eq. (6)); **c.** speckle contrast (C, Eq. (2)); **d.** contrast-to-noise ratio (CNR, Eq. (3)); **e.** comparison of speckle contrast calculated using lines of final tomogram, region A at Fig. 4, with the one obtained using integration of autocorrelation function $\overline{R}_{YY}(k)$, Eq. (16); **f.** autocorrelation function $\overline{R}_{YY}(k)$ as a function of lateral beam deflection. **g., h., i.** averaged cross-sectional images obtained for different values of lateral beam deflection on the sample.

5(i). The cross-sectional image obtained for optimal CNR enables keeping the balance between reasonably high value of contrast C (as for larger 560 µm beam deflection), and high $pSNR$. The same conclusion can be drown from a comparison of the plots presented in Fig. 5(b-d).

Although an optimization of the beam deflection based on CNR plot is possible, it is not feasible in *in vivo* studies, as it requires many measurements with different scanning parameters. Therefore, we suggest using the optimization technique that is based on theoretical results presented in paragraph 2.4. For testing the technique we used the same data which were acquired for the previous experiments. As stated in paragraph 2.4, the standard signal deviation can be calculated either from a fragment of the averaged tomogram or using area under curve of autocorrelation function of A-scans from one segment of data used for averaging, Eq. (16). For data sets acquired with different lateral beam deflections, the speckle contrast calculated from the area under the curve of $\bar{R}_{YY}(k)$ function agrees well with the speckle contrast of the averaged image, as predicted (Fig. 5(e)). To show that the autocorrelation function $\bar{R}_{YY}(k)$ can be used to predict the optimal value of the lateral beam deflection, we calculated the $\bar{R}_{YY}(k)$ functions for 3 data sets with the lateral beam deflections set to 74 µm, 37 µm and 19 µm, respectively (Figs. 5(f) and 5(g)). All the data sets were acquired with 10 µs repetition time (8.6 µs exposure time). The $\bar{R}_{YY}(k)$ function is drawn as a function of deflection amplitude of the scanning beam (Fig. 5(f)). For all three data sets, the plots of $\bar{R}_{YY}(k)$ fall to zero close for deflection amplitude equal approximately to 160 µm, 140µm and 100 µm, which is close to the optimal value for speckle reduction (110 µm), that can be deducted from Fig. 5(d). The observed deviation from the optimal value found for higher amplitudes is connected with the movement the beam on the sample during data acquisition and resulting slower decorrelation of acquired spectra. We believe that such analysis can help to estimate the optimal lateral beam deflection using one measurement, without the need of performing many measurements for large variation of the lateral beam deflection. This method was used to estimate the optimal beam deflection for all *in vivo OCT* images presented in the subsequent section.

3.2. In vivo imaging

In all experiments described in this section we averaged 16 optical A-scans acquired with exposure time of 5 µs. The number of segments and the imaging range in lateral (x) direction were variable. The lateral beam displacement induced by a resonant scanner during acquisition of A-scans has been optimized by the technique described above and was approx. 110µm.

In the first experiment we imaged human finger *in vivo*. The fingernail presented in Fig. 6(a) and Fig. 6(c), and skin from fingertip, shown in Fig. 6(b) and Fig. 6(d), have been chosen as test areas. Figure 6(a) and Fig. 6(b) show one tomogram from the center of the segment, while Fig. 6(c) and Fig. 6(d) show images formed as an average of 16 tomograms. The imaging range was set to 9.4 mm with 2000 segments (Fig. 6(a) and Fig. 6(c)) and 2.35 mm with 5000 segments (Fig. 6(b) and Fig. 6(d)). In the Fig. 6(d) one can observe broadening of the skin surface. This is caused by the averaging of 110 µm thick set of tomograms. Due to the fact that ridges of dermatoglyphs are not perfectly perpendicular to lateral (x) dimension, the edge of the ridge can be shifted on each consecutive tomogram. Such blur on the image will appear when the technique is used on samples with structural details smaller in lateral (y) dimension than applied beam deflection. It has to be noted, however, that such worsening of the resolution appears only in one direction and is fully controlled by the operator of the device who can consciously choose to compromise lateral resolution for speckle contrast decrease or vice versa.
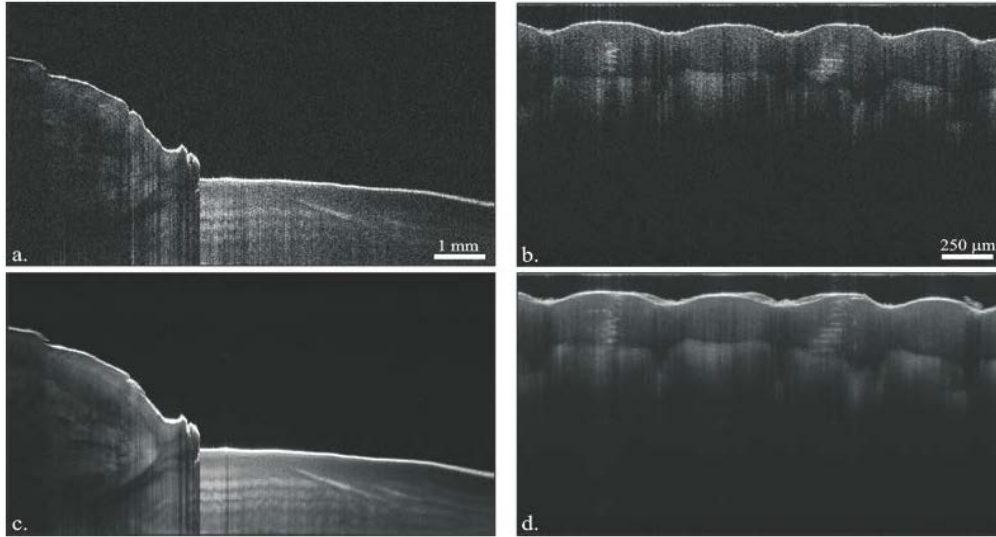
Fig. 6. OCT imaging of the human finger *in vivo*. Fingernail (2000 segments x 16 A-scans, 9.4 mm): **a.** single cross-sectional image, **c**. cross-sectional image with reduced speckle contrast by averaging of 16 A-scans deflected orthogonally to the directions of lateral scanning and beam propagation. Fingertip (5000 segments, 2.35 mm): **b.** cross-sectional image, **d**. cross-sectional image with reduced speckle contrast.
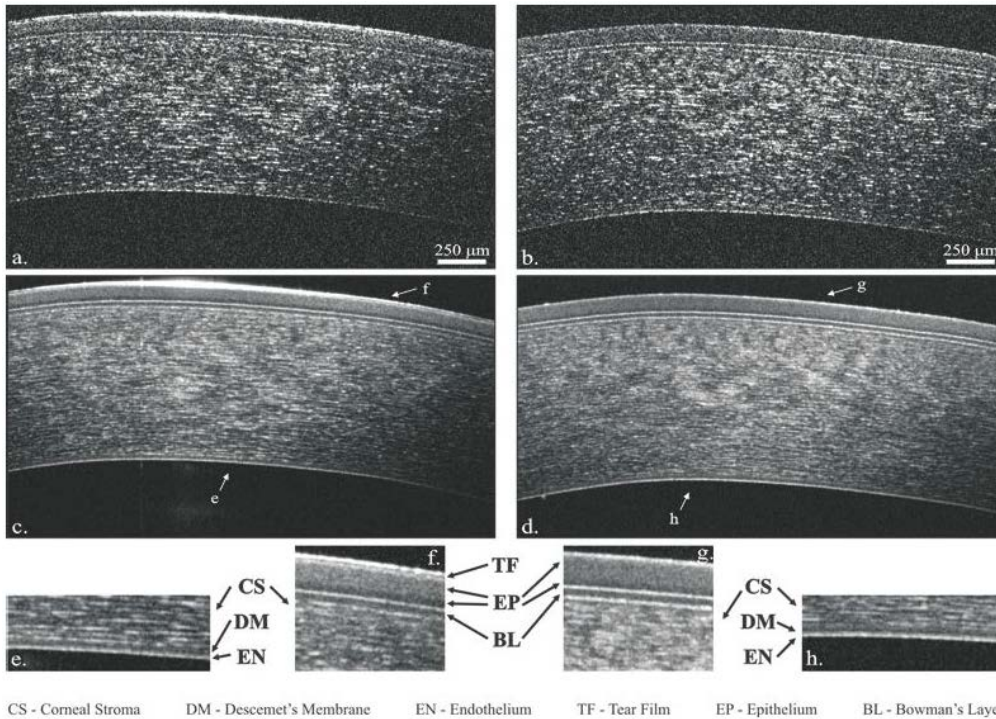

CS - Corneal Stroma   DM - Descemet's Membrane   EN - Endothelium   TF - Tear Film   EP - Epithelium   BL - Bowman's Layer

Fig. 7. Reduction of the speckle contrast in OCT images of the human cornea. Single cross-sectional images: **a.** subject 1, **b.** subject 2. Cross-sectional images with averaged 16 A-scans deflected orthogonally to the directions of lateral scanning and beam propagation (1000 segments, 2.5 mm): **c.** subject 1, **d.** subject 2. Panels **e.-h.** show twice zoomed details of the cornea taken from both subjects.

In the second experiment we applied the speckle reduction technique to image cornea of the human eye of two healthy male volunteers (subject 1: 35 y.o., subject 2: 32 y.o.). The results are shown in Fig. 7. The imaging range was 2.5 mm and images with speckle contrast reduction were constructed with 1000 segments (measurement time: 0.25 s). In Fig. 7 left column presents images obtained from subject 1, and right from subject 2. Figure 7(a) and Fig. 7(b) show a single cross-sectional image selected from the set of data used for averaging, Fig. 7(c) and Fig. 7(d) show images formed as an average of 16 tomograms. Figure 7(e-h) show zoomed details of selected parts of the cross-sectional images with reduced speckle contrast. It is possible to distinguish the tear film in Fig. 7(f). Because the measurement of subject 1 was taken right after the eye blink, the tear film was relatively thick. The cross-sectional images presented in Fig. 7(c) and Fig. 7(d) show a slight change of the imaging contrast within the epithelial layer forming two layers of different reflectivity, as shown in Figs. 7(f-g). Also the Bowman layer is visible with reasonable contrast, which is not so clearly distinguishable in images without reduced speckle contrast. The reconstruction of the stroma in posterior section of the cornea reveals more homogeneous layer close to endothelium, which may indicate the presence of Descemet's Membrane, as can be seen in Fig. 7(e) and Fig. 7(h).

Figure 8 shows the results of the reduced speckle OCT imaging applied to the crystalline lens for the same two subjects as in the previous experiments. The imaging range was set to 7 mm. Figure 8(a) and Fig. 8(b) present a single cross-sectional images selected from the set of data used for averaging. Figure 8(c) and Fig. 8(d) show effects of the speckle reduction. In these cross-sectional images each line is calculated form 16 A-scans deflected in direction perpendicular to both beam propagation and to direction of lateral scanning. Figure 8(e) and Fig. 8(f) show zoomed region of the front part of the lenses with the lens capsule and the epithelium being clearly distinguishable.
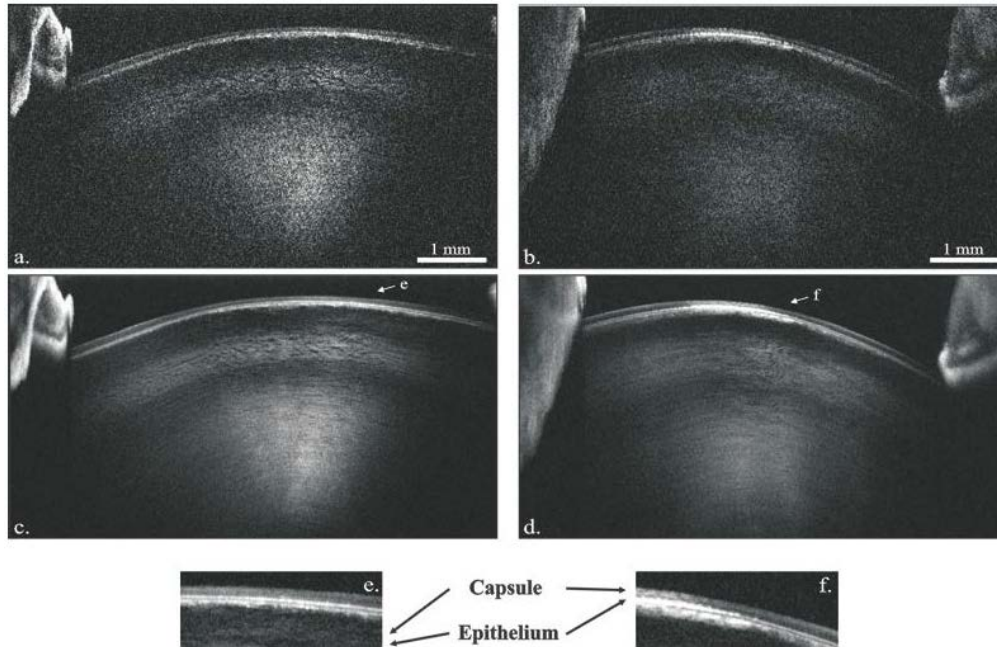

Fig. 8. Reduction of the speckle contrast in OCT images of the human crystalline lens *in vivo*. Single cross-sectional images: **a.** Subject 1, **b.** subject 2. Cross-sectional images with averaged 16 A-scans deflected orthogonally to the directions of lateral scanning and beam propagation (1000 segments, 7 mm): **c.** subject 1, **d.** subject 2. Panels **e.-f.** show twice zoomed details of the lens capsule.
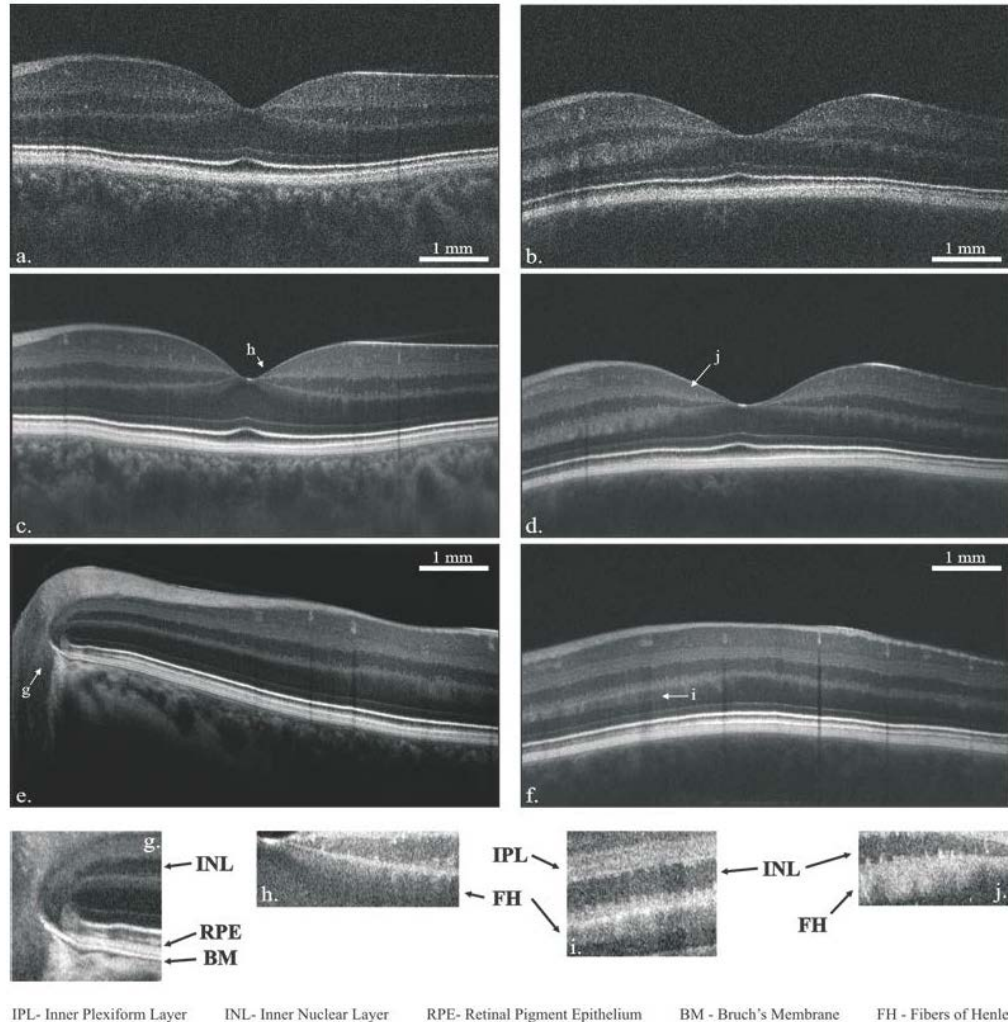
Fig. 9. Reduction of the speckle contrast in OCT images of the human retina *in vivo*. Imaging range: 7 mm. Single cross-sectional images: **a.** Subject 1, **b.** subject 2. Cross-sectional images with averaged 16 A-scans deflected orthogonally to the directions of lateral scanning and beam propagation (2000 segments): **c., e.** subject 1, **d., f.** subject 2. Panels **g.-j.** show twice zoomed details of the retinal cross-sectional images.

To test the speckle contrast reduction we also imaged the human retina. In this case we measured two different eyes form the same subjects as in the previous experiments. For the retinal imaging (presented in Fig. 9) we increased the number of segments to 2000 (total measurement time: 0.5 s, imaging range 7 mm), Standard OCT retinal cross-sectional macular images are demonstrated in Fig. 9(a) and Fig. 9(b). The effect of the speckle contrast reduction is presented in Fig. 9(c) and Fig. 9(d), which was obtained by averaging of 16 A-scans per single line of the image. Figure 9(e) and Fig. 9(f) show another examples of the retinal imaging from the same subjects measured close to the optic disc and at the periphery of the macular region(500 µm superior to the macula). Figures 9(g-j) show zoomed regions of the Fig. 9(c-f). Interestingly, in Fig. 9(g) it is possible to find dark region separating choriocapillaris region from RPE. Border Tissue of Elschnig is clearly visible in Fig. 9(e). We can also find an indication of the presence of Henle fibers (FH) in Fig. 9(h-j). The contrast of the Henle fibers changes with probing beam angle (Fig. 9(d)). In speckle reduced images the

Inner Plexiform Layer (IPL) can be easily distinguished and separated from the Ganglion Cell layer. It is also possible to see a fine structure of this layer, which may reveal more morphological details (Fig. 9(i, c-f)) [31].

In order to demonstrate the improvement in quality of the images acquired using the speckle contrast reduction technique, we gathered the same amount of OCT data with the resonant scanner turned on and off. We used similar averaging procedure for both sets of data. Figure 10 presents a comparison of standard averaging procedure and orthogonal beam deflection averaging for the human cornea and retina. The number of spectra acquired in normal scan was set to 32 000, the A-scans were averaged by 16 to form final image consisting of 2000 lines. Consequently, the amount of data was equal for both averaging techniques. The results are presented in Fig. 10. In the images of cornea acquired using additional beam deflection, presented in Fig. 10(c) and Fig. 10(f), both Bowman's Layer and Epithelium present sharp contours, while in the image acquired with standard averaging approach these structures are strongly disturbed by the speckle noise, Fig. 10(a) and Fig. 10(e). The same difference in image quality is visible in the case of macular imaging. Structural details visible in speckle noise reduced images, presented in Fig. 10(d) and Fig. 10(h), are not distinguishable in the images acquired in standard way due to the presence of the speckle noise, as shown in Fig. 10(e) and Fig. 10(g).
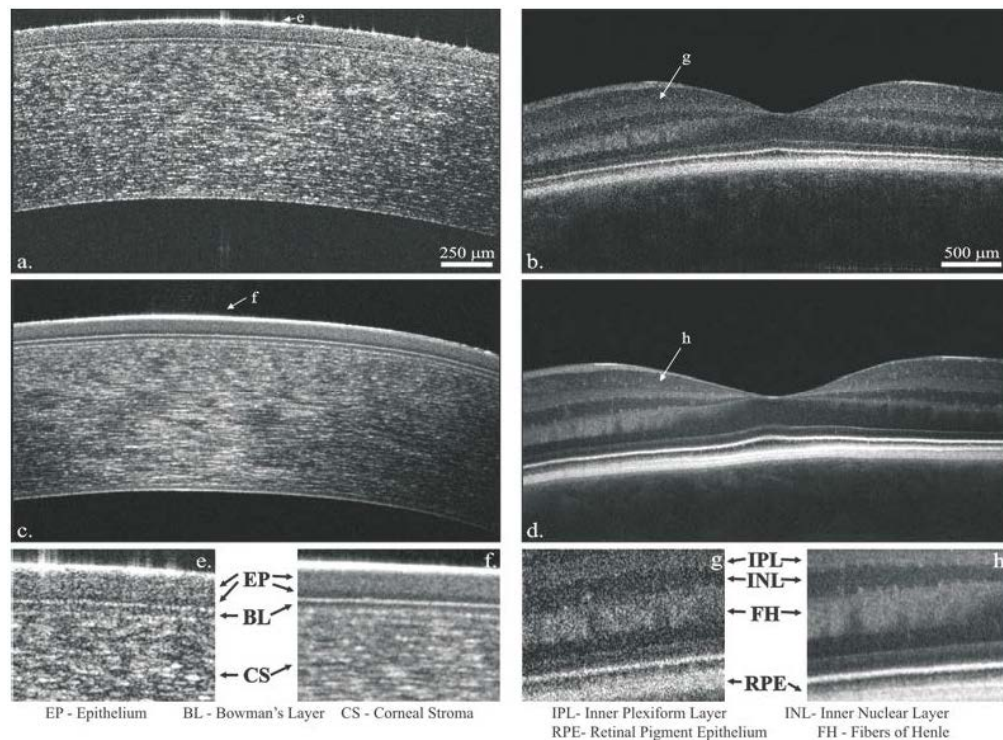

Fig. 10. Comparison of different approach to A-scan averaging. **a., b.** Standard scanning protocol (without lateral deflection), 32 000 A-scans averaged by 16, to form tomograms with 2000 lines. **c., d.** Same amount of data, but acquired with lateral beam deflection. **e., f.** Zoomed anterior part of cornea from similar regions. **g., h.** Zoomed retinal layers from similar regions of the image. See the text for details.

3.3. Resolution and motion artifacts

Averaging of A-scans acquired from distant positions of the light beam on the sample leads to a decrease of lateral resolution. In the case of averaging A-scans within one tomogram the lateral resolution in lateral (x) direction is compromised. In the case of averaging of

tomograms acquired in OCT system equipped with a sample tracking system, the resolution is worsened in both lateral (x) and (y) direction. This is caused by the fact that during long time span between acquisitions of A-scans to be averaged the sample moves in random lateral directions and rotates by random angles. Not all of the motions can be corrected by the tracking system, what makes A-scans to be distributed randomly within an area, which diameter depends on the sample motion amplitude, the performance of the tracking system and the acquisition time of the tomogram.

In the technique proposed the abovementioned problem is minimized, since the time span between the first and last averaged A-scan is at most equal to a half of resonant scanner period, what in our case is 125 µs. Since the velocity of the beam on the sample ranges to hundreds of mm/s, while observed motion velocity of the eye is in the range of single mm/s, the impact of the sample displacement component is negligible as compared to the beam movement.
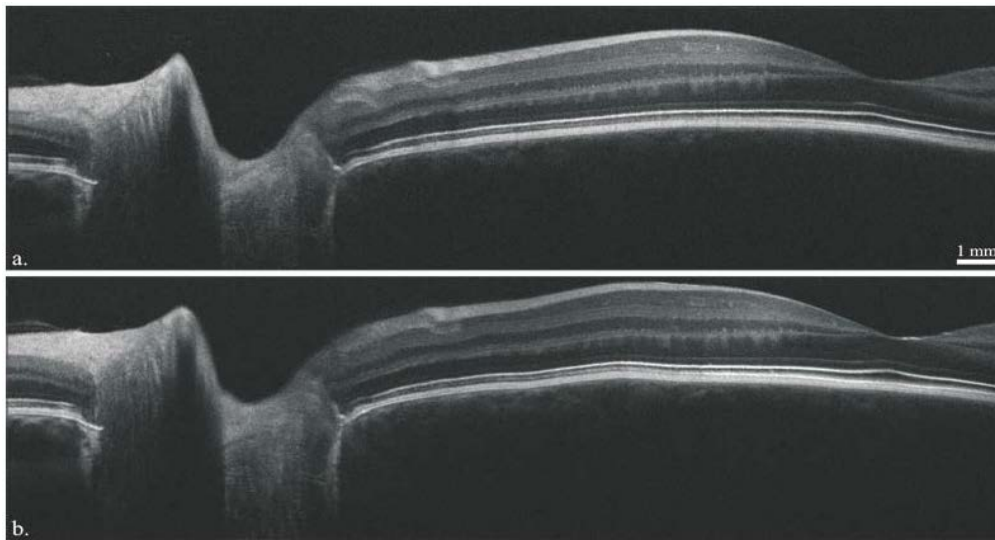

Fig. 11. Panoramic cross-sectional images of the human retina with reduced speckle noise. Imaging range in lateral direction is equal 11.3 mm. **a.** Tomogram composed from 2000 segments. Acquisition time 0.5 s. **b.** Tomogram composed from 5000 segments. Acquisition time 1.25 s.

This technique has also the ability to minimize the influence of the bulk motion in axial direction. In the case of retinal imaging usual bulk motion velocity of human retina is in the range of few millimeters per second. Assuming velocity of 5 mm/s, the shift between the first and last A-scans to be averaged is equal to 0.5µm, which is much less then axial resolution of the system. Axial shift equal to resolution of the system, which is 4.2 µm in tissue, is achieved when bulk motion of the sample reaches velocity of 40 mm/s. As a result, the bulk motion has little impact on A-scan averaging within one segment of data. Figure 11 shows panoramic images of the human retina measured along papillomacular axis obtained with two different number of lines. A slight distortion in retinal shape is visible in the image acquired within 1.25 s, as shown in Fig. 11(b). Similar distortion is not visible in the image presented in Fig. 11(a) acquired in 0.5 s. Such small distortions can be corrected using simple algorithms. The axial resolution within a single A-scans is not affected by the bulk motion.

In the case when the sample is not perfectly laminar along lateral (y) direction, the averaging process can significantly influence the axial resolution of OCT imaging, as shown in Fig. 12(b). This is caused by the shift in axial direction of the A-scans within one segment, what is presented schematically in Fig. 12(a). This resolution drop can be minimized by the numerical tilt correction of the sample, that can be easily performed in post-processing. Each

segment of OCT data with A-scans registered for variable (y) positions (resonant scanner deflection) can be analyzed separately and aligned before averaging, as depicted in Fig. 12(c). The tilt angle can be easily and automatically traced in every data segment. An example of a corrected cross-sectional image is presented in Fig. 12(d).
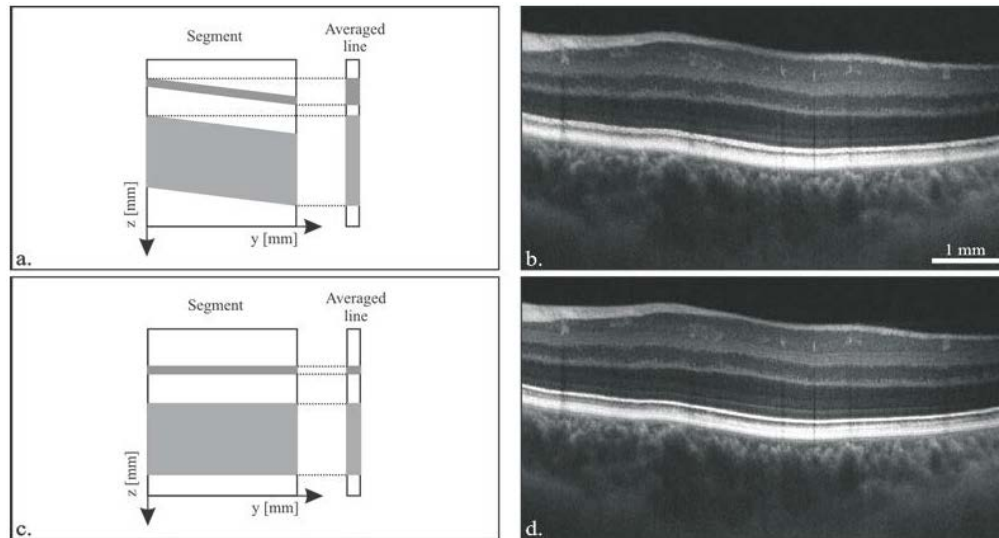

Fig. 12. Correction of tilt distortion. **a.** Schematic drawing of OCT data segment with structure tilted in lateral (y) direction. **b.** Tomogram of human retina in proximity of macula with axial resolution distorted by sample tilt. **c.** Schematic drawing of segment with corrected structure tilt in lateral (y) direction. **d.** Tomogram from b. corrected for the sample tilt.

3.4. Real-time imaging

The data acquisition and display software designed and created by the authors of this paper enables to reduce the speckle contrast in real time and can be used in the *Preview Mode* of our laboratory device. In this mode 6 frames per second consisting of 400 lines build from average of 16 A-scans each were acquired and displayed. Figure 13 presents two frames from a movie (Media 1) acquired during the *Preview Mode*. Fig. 13(a) shows a movie frame obtained when orthogonal beam deflection is minimized, while Fig. 13(b) shows a movie frame obtained when the beam deflection is set to the optimal value.
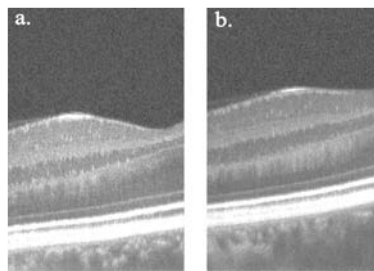

Fig. 13. (Media 1) Movie frames from the *Preview Mode* sequence: **a.** minimized deflection; **b.** optimal beam deflection.

3.5. Doppler imaging

In the technique proposed the lateral beam deflection can be introduced either in lateral (x) or (y) directions. Therefore, it is possible also to set the dense sampling along lateral (x) direction. Such oversampling is sufficient to obtain axial velocity maps of the sample, using

joint Spectral and Time domain OCT [64,69] or using any other Doppler OCT approach. To show the possibility of simultaneous speckle reduction and Doppler imaging, we performed a measurement of the human retina in the proximity of optic nerve head and macula lutea. We acquired 6000 segments over a range of 7 mm (optic nerve head) or 3 mm (macula lutea). Figures 14(a) and 14(b) show structural tomograms with reduced speckle noise. Because of the large number of spectra acquired, the tomograms are slightly distorted in axial direction. Figures 14(c) and 14(d) show averaged Doppler velocity maps created by averaging of Doppler tomograms calculated with the same number of spectral fringes within segments.
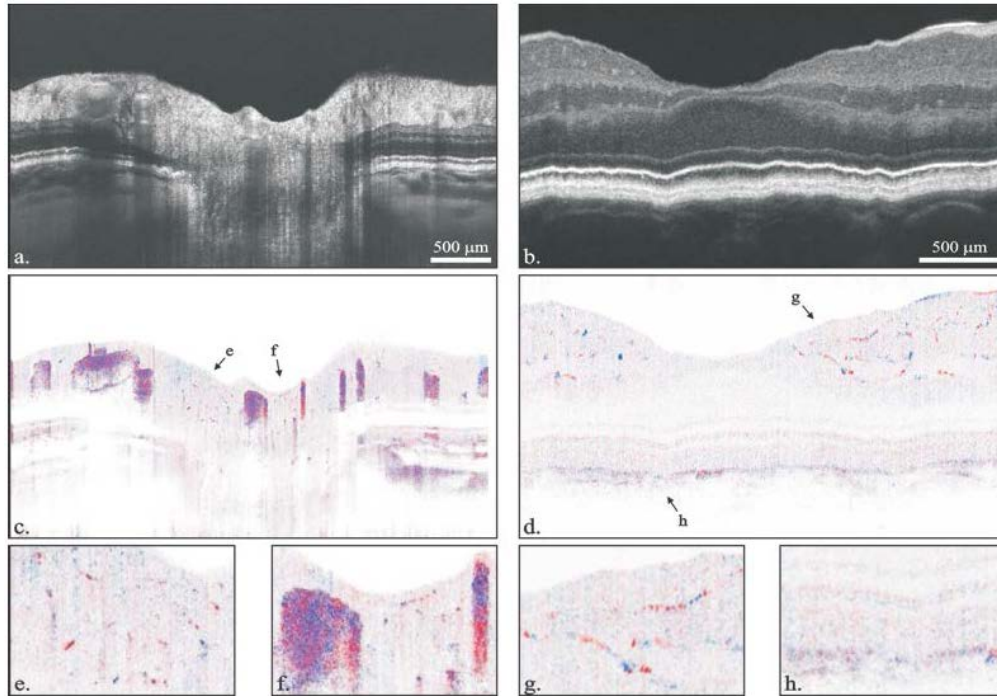

Fig. 14. Doppler imaging using resonant scanner. 6000 segments. **a.** Structural tomogram in proximity of optic nerve head of the human eye. Imaging range: 7 mm. **b.** Structural tomogram in proximity of macula lutea. 6000 segments. Imaging range: 3 mm. **c.** Doppler OCT map of a.; **d.** Doppler OCT map of b. **e-f.** Zoomed areas from c. **g-h.** Zoomed areas from c.

The maximal velocity detectable by Doppler OCT depends on the time span between A-scans, which in our case is equal to segment repetition time $T_{segment} \cong 250 \mu s$, and is equal to approx. $0.6 mm/s$. For that reason, the large vessels present only qualitative information about the flow, which largely exceeds the maximal detectable velocity, as shown in Fig. 14(f). For the same reason, micro capillaries with much lower values of axial velocity are visible in both optic nerve head area, as can be seen in Figs. 14(e-f), and in proximity of macula, presented in Fig. 14(g). For a more complete discussion about Doppler imaging using SOCT setup with additional beam deflection in lateral (y) direction please address our previous work presented in Ref. [64]. In the technique we propose here, the sensitivity to motion is decreased due to the fact that the scanning beam moves with high velocity on the sample. As a result, the velocity noise is increased, and the overall signal to noise ratio decreases. Since the sensitivity of Doppler imaging depends on signal to noise ratio, it is decreased as well. Additionally to velocity related Doppler signal, on Fig. 14(h) one can see the impact of highly scattering Bruch's membrane on scrambling the phase of light, what effects in increased phase noise in that region.

4. Conclusions

In this work we have demonstrated the speckle contrast reduction technique based on spatial compounding of OCT A-scans with high-speed segmented scanning protocol. In our experiments we were able to control and optimize the process of a speckle contrast reduction with preserving relatively high SNR by optimizing Contrast to Noise Ratio value (CNR). Such optimization was possible by precise control of the beam deflection in direction orthogonal to both the direction of lateral scanning and to the direction of light beam propagation. This method works well for structures with laminar morphology like human cornea and retina. We have also demonstrated that it is possible to minimize the axial resolution loss by additional numerical alignment of measured data. Important advantage of this technique is the fact that bulk motion artifacts have minimal impact on the speckle reduction, and the same on the resolution and image quality. We have presented the OCT setup and software which are able to acquire, calculate and display images with reduced speckle contrast in real time. An extra feature of segmented scanning protocols using the resonant scanner is a visualization of retinal micro capillaries. We have demonstrated the applicability of the technique proposed to visualize human skin as well as anterior and posterior parts of the human eye *in vivo*.

In the technique proposed the lateral resolution is different in lateral (x) and (y) direction and equals to approx. 15 µm and 110 µm, respectively. The apparent increase in imaging quality is due to the elongation of lateral point spread function along (y) axis. Therefore, similar effects could be in principle obtained in standard SOCT setup without the use of the resonant scanning system. The same information can be acquired using raster scan with several hundreds of B-scans with galvo-scanners. To obtain an image with significant reduction of the speckle contrast, a number of A-scans covering distance of approx. 110 µm should be averaged, giving one line of a new tomogram with lateral extent in (y) direction. A tomogram composed with lines averaged in such a way will have similar properties as the ones described in the manuscript. There is, however, a problem of bulk motion of the sample, as the time span between B-scans acquisition, and in consequence between new tomogram lines is much larger than in the technique exploiting resonant scanner. As a result, the obtained tomograms may have consecutive lines dispersed in lateral directions. This makes strong limitation in the applicability of such approach to *in vivo* imaging. It can be, however, useful in material or *ex vivo* imaging studies. A potential application of this approach is under investigation now and will be published in near future.